

The Continuum of Drought in Southwestern North America

LUKE A. PARSONS^a

Department of Geosciences, The University of Arizona, Tucson, Arizona

SLOAN COATS

Woods Hole Oceanographic Institution, Woods Hole, Massachusetts

JONATHAN T. OVERPECK

School for Environment and Sustainability, University of Michigan, Ann Arbor, Michigan

(Manuscript received 8 January 2018, in final form 1 June 2018)

ABSTRACT

Drought has severe consequences for humans and their environment, yet we have a limited understanding of the drivers of drought across the full range of time scales on which it occurs. Here, the atmosphere and ocean conditions that drive this continuum of drought variability in southwestern North America (SWNA) are studied using the latest observationally based products, paleoclimate reconstructions, and state-of-the-art Earth system model simulations of the last millennium. A novel application of the self-organizing maps (SOM) methodology allows for a visualization of the continuum of climate states coinciding with thousands of droughts of varying lengths in last millennium simulations from the Community Earth System Model (CESM), the Goddard Institute for Space Studies Model E2-R (GISS E2-R), and eight other members from phase 5 of the Coupled Model Intercomparison Project (CMIP5). It is found that most droughts are associated with a cool Pacific decadal oscillation (PDO) pattern, but persistent droughts can coincide with a variety of ocean–atmosphere states, including time periods showing a warm PDO or weak ocean–atmosphere anomalies. Many CMIP5 models simulate similar SWNA teleconnection patterns, but the SOM analysis demonstrates that models simulate different continuums of ocean–atmosphere states coinciding with droughts of different lengths, suggesting fundamental differences in their drought dynamics. These findings have important implications for our understanding and simulation of the drivers of persistent drought, and for their potential predictability.

1. Introduction

Droughts threaten water and food security, human health, and natural ecosystems (e.g., [Acuna-Soto et al. 2002](#)) and occur across a range of time scales, from seasons to multiple decades. In addition to the risk of natural drought variability, projections from state-of-the-art climate models indicate that future drought in southwestern North America (SWNA; 25°–43°N,

125°–105°W) will likely exceed even the driest decades of the last millennium ([Cook et al. 2015](#)), although this result may be sensitive to the choice of drought metric ([Roderick et al. 2015](#); [Milly and Dunne 2016](#); [Berg et al. 2016](#); [Scheff et al. 2017](#)). Despite the importance of drought, the mechanisms that drive droughts across the full range of time scales on which they occur remain poorly understood. Recent studies indicate that droughts are triggered by a combination of land–atmosphere feedbacks, coupled atmosphere–ocean interactions, external forcing (e.g., volcanic eruptions), and/or random shifts in atmospheric circulation (e.g., [Delworth and Manabe 1989](#); [Gutzler and Preston 1997](#); [McCabe et al. 2004](#); [Seager and Hoerling 2014](#); [Seager et al. 2015](#); [Cook et al. 2016](#); [Stevenson et al. 2015, 2018](#); [Coats et al. 2013b, 2015a,b,c, 2016a,b](#); [Ault et al. 2018](#)). Herein, we address the question of whether the dominant

 Denotes content that is immediately available upon publication as open access.

^a Current affiliation: Department of Atmospheric Sciences, University of Washington, Seattle, Washington.

Corresponding author: Luke A. Parsons, lakp@uw.edu

DOI: 10.1175/JCLI-D-18-0010.1

© 2018 American Meteorological Society. For information regarding reuse of this content and general copyright information, consult the [AMS Copyright Policy](#) (www.ametsoc.org/PUBSReuseLicenses).

processes driving drought change as the temporal persistence of drought increases.

A full characterization of the mechanisms underlying drought requires a sufficiently large sample, including a sample of relatively rare decadal and multidecadal droughts. The instrumental interval is at most 150 years, so actual observations of the climate system cannot provide such a sample. However, ensemble simulations of the last millennium (e.g., [Otto-Bliesner et al. 2016](#)) provide tens of thousands of simulation years containing thousands of SWNA droughts. Analyzing the ocean–atmosphere conditions associated with these droughts is a “big data problem” that cannot be fully addressed with simple correlation or composite maps. For the first time, we employ a self-organizing maps (SOM) analysis approach ([Kohonen 1982](#)) to these model ensembles, which allows for a more nuanced examination of the continuum of ocean–atmosphere conditions that coincide with droughts of varying lengths in SWNA.

Models provide imperfect representations of the climate system and the atmosphere–ocean drivers of drought (e.g., [Flato et al. 2013](#)). Likewise, each model simulates the climate differently, so differences in drought dynamics across models are expected, and it is important to determine if model-based inferences are robust across simulations. Until recently, analyses like those proposed here were not possible because of the computational expense of running long (>500 yr) model simulations, let alone single and multimodel ensembles of these simulations. For the first time, such ensembles of simulations are readily available, although their drought dynamics have not yet been analyzed and compared in a systematic framework. These ensembles include the National Center for Atmospheric Research (NCAR) Community Earth System Model (CESM) Last Millennium Ensemble (LME) (over 12 000 years of “full forcing” output; [Otto-Bliesner et al. 2016](#)), the National Aeronautics and Space Administration (NASA) Goddard Institute for Space Studies Model E2 coupled with the Russell ocean model (GISS-E2-R) Last Millennium (over 9000 simulation years; [Schmidt et al. 2012, 2014](#)), and the full suite of Last Millennium (LM) simulations from phase 5 of the Coupled Model Intercomparison Project (CMIP5). The nearly 30 000 simulation years across these single and multimodel ensembles are analyzed here to better understand how the characteristics, occurrence, and dynamics of drought across time scales differ based on different representations of the coupled ocean–atmosphere system ([Taylor et al. 2012](#); [Schmidt et al. 2012](#)). Observations and paleoclimate records are also analyzed in concert with these simulations, and a discussion of how structural biases within these models may limit the real-world relevance of the results is included in [sections 3 and 4](#).

Previous research has focused on the roles of atmosphere ([Cayan et al. 1998](#); [Seager et al. 2015](#); [Stevenson et al. 2015](#)), coupled ocean–atmosphere ([Trenberth et al. 1988](#); [Cayan et al. 1998](#); [Meehl and Hu 2006](#); [Seager 2007](#); [Conroy et al. 2009](#); [McCabe-Glynn et al. 2013](#); [Seager and Hoerling 2014](#); [Routson et al. 2016](#)), coupled land–atmosphere (e.g., [Langford et al. 2014](#); [Delworth and Manabe 1989](#); [Gutzler and Preston 1997](#)), and external forcing (e.g., [Stevenson et al. 2018](#); [Coats et al. 2015b](#)), including from greenhouse gases (e.g., [Dai 2013](#); [Wang et al. 2014](#); [Swain et al. 2014](#); [Cook et al. 2014, 2015](#); [Diffenbaugh et al. 2015](#); [Williams et al. 2015](#); [Ault et al. 2016](#); [Woodhouse et al. 2016](#); [Udall and Overpeck 2017](#)), in driving drought across a range of time scales. Although previous work has highlighted the possible ocean–atmosphere drivers of single drought events (e.g., [Seager et al. 2015](#)) or composites of drought events (e.g., [Meehl and Hu 2006](#)), here we take a novel approach to studying drought by explicitly examining the continuum of SWNA drought across time scales and the corresponding coupled ocean–atmosphere conditions underlying droughts as a function of their length. We choose to focus on SWNA because widespread drought conditions lasting decades have been well documented in the paleoclimate record and have also received considerable attention in the climate science literature (e.g., [Cook et al. 2007, 2016](#); [Coats et al. 2015a,b](#)). We seek to answer the following questions about droughts ranging from years to multiple decades in SWNA:

- 1) What is the risk of interannual to multidecadal SWNA drought over the last millennium in the latest Earth system model data (e.g., CESM LME, GISS-E2-R LM, and CMIP5 LM) and gridded paleoclimate reconstructions [e.g., the North American Drought Atlas version 2a (NADAv2a)] ([Cook et al. 2007](#); [Otto-Bliesner et al. 2016](#); [Taylor et al. 2012](#))?
- 2) Are the same oceanic and atmospheric conditions associated with droughts across these interannual to multidecadal time scales (e.g., [Dettinger et al. 1998](#)) in the CESM and across all CMIP5 LM models? For example, do persistent La Niña–like conditions in the tropical Pacific (e.g., [Cayan et al. 1999](#); [McCabe and Dettinger 1999](#); [Seager 2007](#); [Seager et al. 2008](#); [Cole et al. 2002](#)) and an atmospheric blocking “ridge” (e.g., [Swain 2015](#); [Wang et al. 2014](#)) lead to all droughts, regardless of time scale?

2. Data and methods

a. Drought in southwestern North America

We choose to focus on SWNA (25°–43°N, 125°–105°W) because of the prevalence of extended drought

TABLE 1. Model names, experiment types, and variables [surface temperature (TS), precipitation (PR), geopotential height (ZG), and Palmer drought severity index (PDSI)] used in analyses. Historical = 1901–2005 CE; CMIP5 Last Millennium simulations (past1000) = 850–1850 CE. (Expansions of acronyms are available online at <http://www.ametsoc.org/PubsAcronymList>.)

Model and run	Experiment	Forcing	Variables	<i>N</i>
NCAR CESM1(CAM5) (runs 2–13)	Last Millennium Ensemble, Historical	All	pmPDSI, PR, TS, ZG	12
NCAR CCSM4	past1000, Historical	All	PR, TS, ZG	1
CSIRO Mk-3L-1.2	past1000, Historical	All	PR, TS, ZG	1
FGOALS-g1	past1000	All	PR, TS, ZG	1
FGOALS-g2	Historical	All	PR, TS, ZG	1
FGOALS-s2	past1000, Historical	All	PR, TS, ZG	1
GISS-E2-R r1i1p121, p122, p1221, p123, p124, p125, p126, p127, p128	past1000, Historical	All (varying combinations)	PR, TS, ZG	9
HadCM3	past1000, Historical	All	PR, TS, ZG	1
IPSL-CM5A-LR	past1000, Historical	All	PR, TS, ZG	1
MPI-ESM-P	past1000, Historical	All	PR, TS, ZG	1
MRI-CGCM3	past1000, Historical	All	PR, TS, ZG	1

in this region in paleoclimate data (e.g., Cook et al. 2007; Herweijer et al. 2007), and the strong connection between hydroclimate in SWNA and the tropical Pacific, and to maintain consistency with previous literature (e.g., Coats et al. 2013b, 2015b). We calculate droughts over land for the SWNA region by averaging a hydroclimate variable over the region to produce a regional mean time series; a drought begins after two consecutive years of anomalies below the mean of the full SWNA time series and continues until two consecutive years of anomalies above the mean (e.g., Herweijer et al. 2007; Coats et al. 2013b). In addition to quantifying the length of each drought, we also integrate precipitation (PR) during each of these droughts to obtain a “severity” metric.

We use annual PR to calculate the drought intervals used in the SOM analysis. However, we also employ a number of different drought metrics to assess the consistency of the results based on choice of hydroclimatic variable. We show that model-based distributions of drought length using annual PR and the Palmer drought severity index (PDSI; Palmer 1965) are similar in SWNA. We choose PR to calculate drought intervals for all CMIP5 LM simulations because all CMIP5 models provide a consistent and comparable PR variable. By contrast, not all CMIP5 models provide the variables necessary to calculate PDSI, and soil water tends to be inconsistent and thus difficult to compare across models (e.g., due to different resolutions in different land models). In the CESM, we have also compared annual mean PDSI to 30-cm soil moisture, 2-m soil moisture, and PR and find that the variability in these three variables is similar to PDSI over the last millennium (not shown). We also compare drought occurrence in the CESM June–August (JJA) averaged PDSI with the North American Drought Atlas PDSI (Cook et al.

2008); seasonal PDSI as well as annual PDSI and PR drought length distributions in the CESM tend to overlap with the seasonal NADA PDSI drought length distributions.

b. Self-organizing maps

In this study, a self-organizing maps–based analysis is used to characterize the continuum of ocean–atmosphere conditions coinciding with SWNA drought across time scales in the CESM LME, GISS-E2-R LM, and CMIP5 LM simulations (Table 1). The SOM analysis classifies the thousands of ocean–atmosphere states coinciding with droughts in SWNA in these simulations into a smaller set of representative states. Specifically, we use the SOM method to classify annual mean 250-mb (1 mb = 1 hPa) geopotential height patterns during SWNA droughts (>1 yr in length) in these model simulations. We also “track” whether certain representative ocean–atmosphere states are preferentially associated with longer (decadal–multidecadal; ≥ 10 yr in length) or shorter (subdecadal; <10 yr in length) droughts. This methodology provides a novel perspective on the *continuum* of ocean–atmosphere states coinciding with drought across the time scales on which it occurs. Although more commonly used correlation and compositing methods are valuable for visualizing climate information in a condensed manner (e.g., Meehl and Hu 2006), the SOM analysis allows us to specifically visualize the continuum of states that coincide with droughts of different lengths. Here we present a brief overview of the SOM methodology, but further details about the methodology and its application to climate data can be found in Johnson et al. (2008).

SOMs are a clustering approach in which the similarity of *N*-dimensional patterns from a set of samples is maximized, such as two-dimensional (latitude and

longitude) geopotential height or surface temperature patterns (e.g., Cavazos 2000; Cavazos et al. 2002; Hewitson and Crane 2002; Cassano et al. 2007; Reusch et al. 2007; Johnson et al. 2008). Each cluster in a SOM is associated with a single representative pattern (the SOM “map”), which approximates the mean of all samples assigned to that cluster. Each SOM map thus represents a generalization of all the observed physical patterns in the input data that match it best, which is a significant advantage over empirical orthogonal function analysis (EOF) because EOFs may not represent physical patterns (Reusch et al. 2005; Liu et al. 2006; Johnson et al. 2008). SOMs differ from traditional clustering algorithms because the maps output from the analysis are organized in a grid structure or topology, the size and shape of which is user defined. This grid structure can be of any dimensionality but is typically two-dimensional for SOM applications to patterns of climate variability (e.g., Hewitson and Crane 2002; Johnson et al. 2008; Gibson et al. 2017).

To illustrate the continuum of atmospheric circulation patterns associated with SWNA drought across time scales, we use the SOM method to classify the composite annual mean 250-mb geopotential height anomalies for all droughts (>1 yr in length) in the CESM LME, GISS-E2-R LM, and CMIP5 LM simulations. After conducting the SOM analysis on the 250-mb geopotential height anomaly fields, we also composite the annual mean surface temperature (TS) anomaly for all droughts associated with each SOM map to determine the sea surface temperature (SST) boundary conditions underlying the geopotential height anomaly fields. The use of 250-mb geopotential height anomalies in the region around North America (15° – 80° N, 120° E– 360°) is chosen because these upper-level atmospheric anomalies are indicative of the atmospheric circulation patterns directly “causing” droughts (e.g., Seager et al. 2005; Wang et al. 2014; Trenberth et al. 1988; Latif and Barnett 1994; Swain 2015). We conduct the SOM analysis separately for each model simulation (CMIP5) or single model ensemble (CESM LME and GISS-E2-R LM). These analyses yield 11 separate SOM 4×3 map grids (one for the CESM LME, one for the GISS-E2-R LM, and one for each CMIP5 LM simulation), resulting in clusters of droughts from a given simulation that are associated with similar patterns of geopotential height anomalies (see further details below).

The user chooses the size of the grid structure in a SOM analysis; here we choose a 4-map by 3-map panel (4×3 grid) to attempt to span the full sample space (e.g., the full continuum of oceanic and atmospheric conditions that coincide with SWNA drought; Fig. 1). The 4×3 SOM maps in Fig. 1 show the continuum of

states between the warm and cool phases of the dominant modes of coupled atmosphere–ocean variability that affect SWNA drought: the Pacific decadal oscillation (PDO), El Niño–Southern Oscillation (ENSO), and Atlantic multidecadal variability or oscillation (AMV/AMO) (e.g., McCabe et al. 2004; Conroy et al. 2009; Coats et al. 2015a,b). Within the grid structure, SOMs group maps with similar patterns close to one another, so SOM maps (and the underlying geopotential height patterns for each drought assigned to that SOM map) influenced by same-signed tropical Pacific (e.g., El Niño and La Niña) and extratropical Pacific and Atlantic surface temperature anomalies tend to be collocated in one area of the grid.

For example, Fig. 1 shows a 4×3 grid of maps from a SOM analysis conducted on composite annual mean 250-mb geopotential height anomalies during SWNA droughts in the CESM LME. The maps in the bottom row of Fig. 1 resemble a cool PDO, and the maps in the top row show a warm PDO. The left column of maps tends to have a cool eastern tropical Pacific (La Niña-like), and the right column shows a cool western tropical Pacific (“neutral” or El Niño-like). Furthermore, maps in the top-right corner of Fig. 1 tend to show weak TS and geopotential height anomalies, but maps closer to the bottom exhibit stronger anomalies. Adjacent maps represent gradients between the dominant patterns represented in the corners; therefore, maps next to one another in Fig. 1 may appear quite similar. The numbers displayed above (below) each SOM map indicate the total (decadal–multidecadal) number of droughts and the associated percent out of the total (decadal–multidecadal) number of droughts that are assigned to that SOM map.

We have systematically tested smaller (e.g., 2×2) through larger (e.g., 8×8) SOM structures. Different SOM grid shapes (e.g., square or rectangular) and sizes (e.g., 4 or 5 rows or columns) produce relatively consistent results because they group different phases of the relevant climate modes in different corners (e.g., Johnson et al. 2008; Gibson et al. 2017).

c. Instrumental-based data

We examine drought in SWNA during the historical era (1901–2005 CE; hereafter all dates are CE unless otherwise specified) using annually integrated PR from the instrumental observation-based GPCCv7 (Schneider et al. 2014) and mean JJA self-calibrating PDSI (scPDSI) from Dai et al. (2004). We also correlate annual mean HadISST (Rayner et al. 2003) SST and NOAA Twentieth Century Reanalysis (20CR; version 2c) 250-mb geopotential height data (Compo et al. 2011) with SWNA GPCCv7 annually integrated PR (Fig. 2). The linear trend

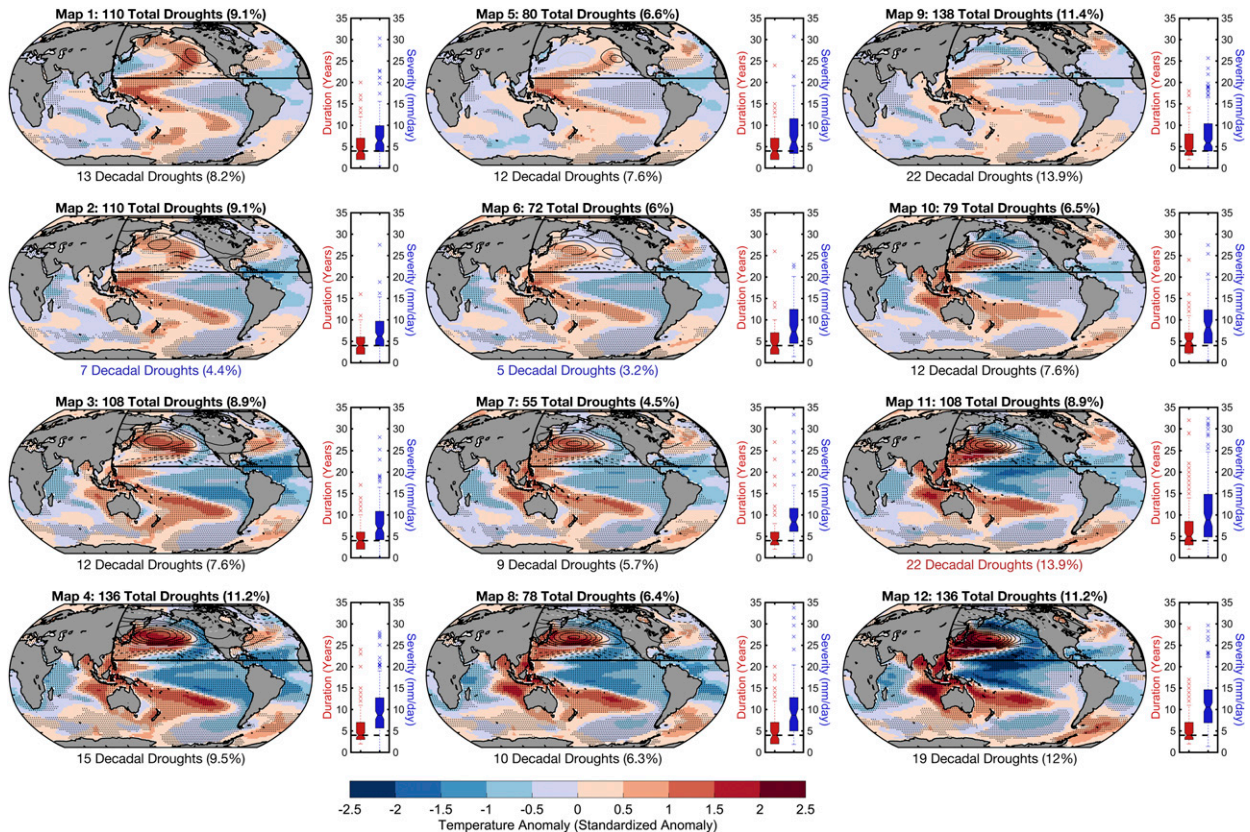


FIG. 1. 4×3 SOM maps of 250-mb geopotential height (contour lines) and associated surface temperature anomalies (shading) from the CESM LME. Panels to the right of each map show the associated distributions of drought length (red boxplots) and severity (blue boxplots). Numbers above maps indicate the total number of droughts (and their associated percentage of $N = 1210$ droughts) associated with each SOM map. Numbers below the maps indicate the total number of decadal–multidecadal (>10 yr; $N = 158$ total) droughts associated with the SOM map. Decadal drought numbers and percentages are shown in red (blue) if the associated geopotential height anomaly pattern is significantly more (less) likely to be associated with decadal–multidecadal droughts than subdecadal droughts (see main text for methods). The contour interval for 250-mb geopotential height anomalies is 0.3 (standardized anomalies), with solid black lines indicating positive anomalies and dotted black lines indicating negative anomalies. Stippling over shaded TS (and black contours for geopotential height) marks regions where the anomalies in the SOM exceed anomalies from a random draw of time segments in the last millennium (see main text for methods). The horizontal dashed reference line in the boxplot panels indicates median drought length from all 1210 droughts in the analysis. The black line in the maps outlines the region of geopotential height anomalies used in the SOM analysis. On boxplots, the central mark is the median, the edges of the box outline the inner quartiles, and the outliers are plotted as individual points outside the whiskers.

(1901–2005) is removed from all time series before correlation calculations. We choose the 1901–2005 time interval for the “historical” analysis because this time interval allows us to directly compare instrumental observation-based datasets to the CMIP5 historical simulations (Taylor et al. 2012).

d. Paleoclimate data

We use the updated North American Drought Atlas version 2a (Cook et al. 2008) reconstructed PDSI. The NADAv2a data are interpolated onto a 2.5° latitude \times 2.5° longitude grid of JJA-average PDSI values for the United States, parts of Canada, and northern Mexico, spanning the years 0–2006. Here we use years 850–1850

for the “last millennium” and years 1901–2005 for the “historical era” continuums of drought length (Fig. 3). More information about this dataset and recent updates can be found in Cook et al. (2014).

e. Earth system model data

Multiple metrics are used to analyze the Earth system model (ESM) output. For instance, we use the JJA Penman–Monteith PDSI (pmPDSI; Jacobi et al. 2013; Stevenson et al. 2016) to compare the continuum of SWNA drought lengths in the ESMs with the JJA PDSI from the NADAv2a. For the SOM analysis we utilize annually integrated PR for better comparisons across all CMIP5 LM models. However, to check the consistency

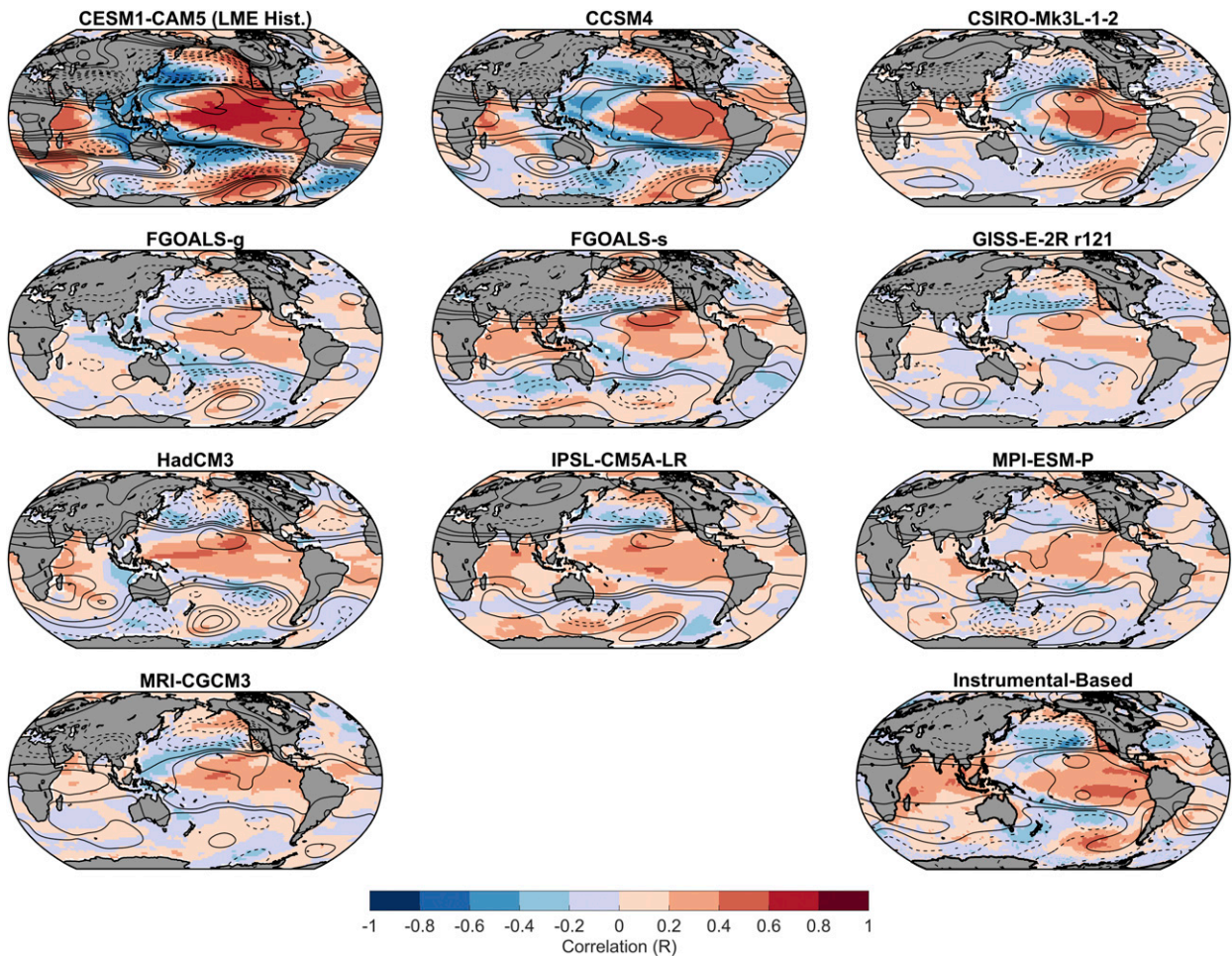


FIG. 2. Correlations among annual PR averaged over SWNA and annual surface temperatures over oceans (shading) and annual 250-mb geopotential height (contour lines) between 1901 and 2005. Map (bottom right) shows correlations among GPCCV7 precipitation averaged over SWNA and annual HadISST sea surface temperatures (shading) and Twentieth Century Reanalysis 250-mb geopotential height (contour lines) between 1901 and 2005. Remainder of maps show correlations in the CESM LME and CMIP5 historical simulations that conducted the past1000 experiment (Table 1). The black box in the maps outlines the SWNA (25° – 43° N, 125° – 105° W) region used throughout this manuscript. Solid (dashed) black contour lines indicate positive (negative) correlations with geopotential height.

of our results, we have also replicated the SOM analysis using annual mean pmpDSI to define SWNA drought intervals in the CESM LME (not shown) and find a minimal difference in our results when compared to a SOM analysis conducted on drought intervals defined using annually integrated PR (Fig. 1).

We use surface temperature and 250-mb geopotential height data to examine the ocean–atmosphere conditions during droughts of various lengths in the CESM LME, GISS-E2-R, and CMIP5 LM simulations (see previous section). We remove the annual cycle and normalized the data at each grid point in the 250-mb height and TS fields. We then calculate the annual mean at each grid point and remove the global mean to maximize the signal from internal variability in the data (e.g., to remove short-lived cooling from volcanic eruptions).

We mask out the land TS values before removing the global mean TS to focus the analysis on the relationship between SST patterns and drought in SWNA. We also correct all geopotential height and TS fields for latitude-dependent gridbox size before all calculations.

We composite 250-mb geopotential height anomalies during each drought interval for input to the SOM analysis, but this averaging tends to smooth (minimize) anomalies during longer droughts and, by comparison, magnify the anomalies during shorter droughts. To correct for the effects of averaging time periods of different lengths to produce the inputs for the SOM analysis (e.g., the composite corresponding to a 2-yr vs a 30-yr drought), we calculate the effect of smoothing on the standard deviation of the geopotential height and TS fields. We then apply this smoothing correction factor to

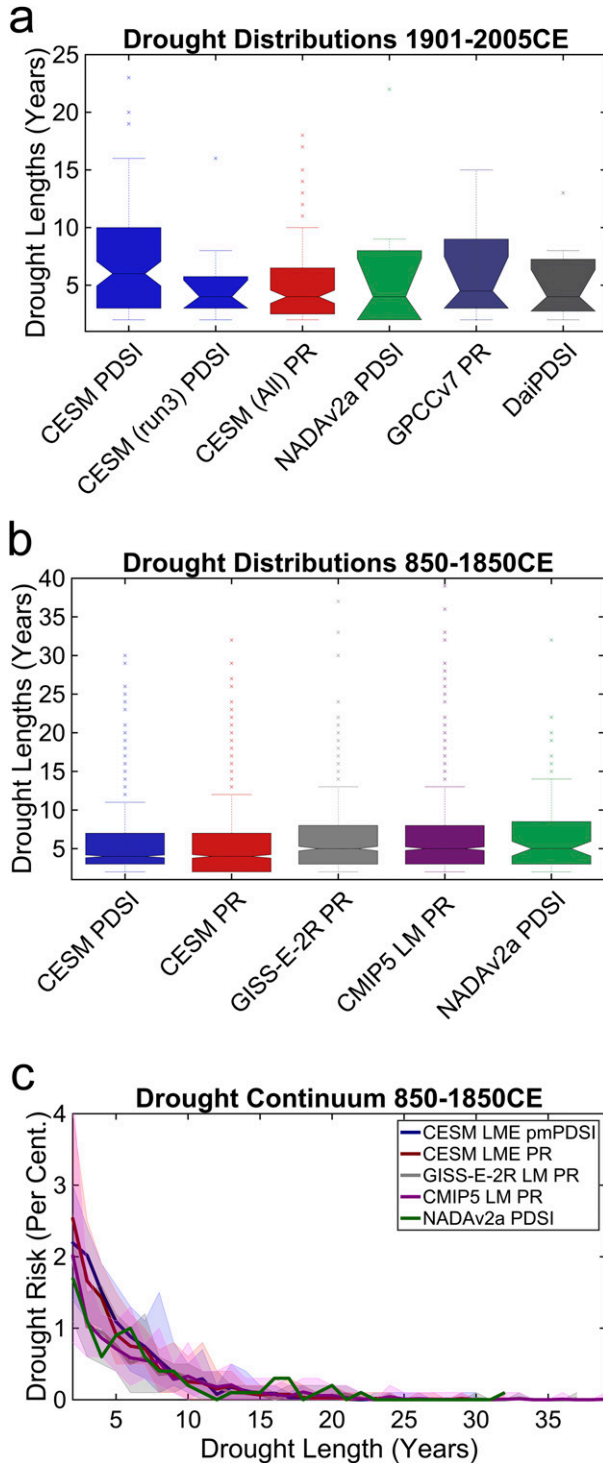


FIG. 3. Drought distributions over the historical (1901–2005) and last millennium (850–1850) time periods. Boxplots show (a) historical distributions of drought length in the CESM LME (pmPDSI), the NADAv2a (PDSI), GPCCv7 (precipitation), and Dai scPDSI, and (b) distributions of drought lengths during the last millennium in the CESM LME (annual PDSI), CESM LME (annual PR), GISS-E2-R (annual PR), CMIP LM (annual PR), and

each grid point before conducting the SOM analysis. This approach normalizes the input geopotential height anomalies so that the magnitudes of anomaly patterns during shorter drought periods are not more heavily weighted than the magnitudes of the patterns during longer droughts in the SOM analysis.

f. Monte Carlo analysis of the dynamics of SWNA drought across time scales

One goal of using this SOM approach is to determine if the ocean–atmosphere conditions driving droughts are different across the varying time scales on which these droughts occur. To do so, we use a Monte Carlo analysis to test if certain SOM maps are preferentially associated with subdecadal versus decadal–multidecadal drought intervals. In this analysis, we conduct a “random draw” of X subdecadal drought intervals 1000 times (where X is the number of decadal–multidecadal drought intervals: 158 in the CESM LME and 147 in the GISS-E2-R) and then calculate the Euclidean distance for each of the X randomly drawn composite geopotential height patterns with each map in the 4×3 SOM corresponding to all drought intervals (section 2b). The minimum Euclidean distance determines to which of these SOM maps a randomly drawn subdecadal drought interval is most closely related. We then calculate the percent of these randomly selected subdecadal drought intervals that are most closely associated with each SOM map. This analysis produces 1000 values of the percent association of subdecadal drought intervals with each of the 4×3 SOM maps, and the 5th and 95th percentiles of these values are used to determine if significantly more or fewer decadal–multidecadal droughts are associated with each SOM map. SOM maps “significantly” more likely to be associated with decadal–multidecadal (subdecadal) drought intervals are shown in red (blue) text in Fig. 1.

We also test whether the geopotential height anomalies in each SOM map and the TS anomalies associated with that SOM map are significantly different than a random draw of these variables in the CESM LME and GISS-E2-R LM (stippling in SOM figures). To conduct this analysis, we first determine the number of droughts and lengths of the drought intervals represented in each

the NADAv2a (JJA PDSI). (c) The mean per centum drought risk as a function of drought length in each of these data sources (CESM LME PDSI, CESM LME PR, GISS-E2-R LM PR, CMIP5 LM PR, and NADAv2a PDSI). Shading outlines maximum and minimum values in individual simulations from each model ensemble.

SOM map, then randomly draw and average combinations of these numbers of TS and geopotential height anomalies 1000 times. We then calculate the 5th and 95th percentiles of these random draws and stipple regions in the SOM figures where the anomalies in the SOM fall outside these values.

3. Results and discussion

a. Model validation: SWNA drought and teleconnections in the twentieth century

A comparison of the distribution of drought lengths in SWNA during the historical era (1901–2005 CE) among the CESM and various instrumental-based data products suggests that the CESM simulates the observed distribution of drought length relatively well (Fig. 3a). The median drought length in all 12 CESM simulations during the historical interval is about six years, and the median drought length in the observation-based datasets are all less than five years. However, the CESM LME shows more decadal–multidecadal “outliers” than any of the instrumental-based data products. The instrumental record may not provide enough data to capture the full continuum of hydroclimatic variability in SWNA (e.g., Woodhouse and Overpeck 1998; Cook et al. 2004; Stahle et al. 2007; Ault et al. 2014, 2018; Stevenson et al. 2018), so we also compare the distribution of droughts in one CESM LME simulation (run 3) to the instrumental record and find that the median drought length and overall distribution of drought length in one CESM LME run overlaps with observations (Fig. 3a). We also compare drought length distributions in the CESM LME and CMIP5 LM simulations to drought distributions in the NADAv2a in section 3b (Fig. 3b).

SST boundary conditions in the tropical Pacific are known to play a role in driving atmospheric circulation anomalies and thus droughts in SWNA (e.g., Bjerknes 1969; Cayan and Peterson 1989; Cayan et al. 1998; Trenberth et al. 1998; Seager et al. 2005; Coats et al. 2013a). A comparison of the correlations among SWNA hydroclimatic variability and global SSTs and 250-mb geopotential height anomalies in instrumental observation-based data and the CESM (Fig. 2) suggests that the CESM captures the spatial pattern of the SWNA teleconnection, but that the CESM shows a stronger teleconnection than is observed (Fig. 2). The GISS-E2-R also realistically simulates the spatial pattern of the SWNA-SST and 250-mb geopotential height teleconnections, but overall SWNA PR in the GISS-E2-R shows a weaker relationship with SST and atmospheric circulation. The other CMIP5 LM models used in this

analysis show similar patterns, but the magnitude of the pattern in the CESM is also stronger than the magnitude of this pattern in most other models (Fig. 2). Importantly, the amplitude of ENSO variability is too strong in the CESM (e.g., Stevenson et al. 2016; Parsons et al. 2017), and thus there is a possibility that the dynamics underlying hydroclimatic variability in this model may disagree with observations (e.g., Ault et al. 2013; Stevenson et al. 2015; Otto-Bliesner et al. 2016). Further analysis of the CESM LME model performance can be found in Otto-Bliesner et al. (2016) and Stevenson et al. (2016, 2017), and a discussion of how this bias may impact the interpretation and real-world relevance of our results is included in section 4.

b. Last millennium SWNA drought length continuum

The simulated annual pmPDSI and PR drought length continua are similar to one another and to the paleoclimate-based NADAv2a JJA PDSI (Fig. 3b). The overall distribution and continuum of drought lengths in the CESM LME generally overlap with the NADAv2a (Coats et al. 2015b; Stevenson et al. 2017). The CESM LME, GISS-E2-R LM, CMIP5 LM, and paleoclimate data tend to show that the region experiences distinct drought intervals lasting 2–3 years at least twice per century, intervals lasting 5 years about once per century, intervals lasting 5–10 years about once every other century, and a decadal–multidecadal drought interval once every few centuries (Fig. 3c). The NADAv2a indicates the region has a lower risk of interannual drought (2–4 years in length) and higher risk of decadal drought (15–20 years in length) than the model ensemble means. However, the drought length distributions of individual simulations within these ensembles show better agreement with the NADAv2a distribution (shading in Fig. 3c).

c. CESM LME SOM analysis

A combination of internal atmospheric variability and oceanic forcing from the tropical and extratropical Pacific and Atlantic may help drive droughts lasting from years to decades (Cayan and Peterson 1989; Cayan et al. 1998; Seager et al. 2005; Seager and Hoerling 2014; Coats et al. 2015b; Stevenson et al. 2015). However, the continuum of atmosphere–ocean conditions that leads to drought across these time scales has not been studied. Here we find that two dominant upper-atmospheric circulation patterns (250-mb height anomalies) tend to coincide with both subdecadal and decadal–multidecadal drought intervals in SWNA: 1) a ridge (e.g., Green 1977) centered off the coast of western North America, south of Alaska and extending over SWNA (e.g., Seager et al. 2005; Wang et al. 2014; Swain

2015); and 2) a ridge centered over the North Pacific gyre, east of the Japan Current/Kuroshio Extension (e.g., McCabe-Glynn et al. 2013). Both shorter and longer droughts tend to be associated with these patterns, suggesting that SWNA droughts on all time scales (subdecadal–multidecadal) are associated with similar atmospheric ridge patterns over the northwest Pacific in the CESM LME (contour lines in Fig. 1), but the more persistent droughts tend to coincide with larger positive geopotential height anomalies over the Kuroshio Extension region (right, bottom panels in Fig. 1). The ridge patterns over the Pacific in these composites represent a combination of multiple distinct, shorter-time-scale atmospheric circulation patterns (e.g., Cayan et al. 1998). In this analysis, we show the mean of these shorter-lived patterns during each drought interval. These composite climate states are thus not indicative of one persistent climate state during each drought, but rather the differences in composites can be interpreted as capturing a different set of these shorter-time-scale atmospheric circulation patterns.

In the CESM, the drought intervals assigned to a specific SOM map tend to also have consistent underlying surface temperature “boundary” conditions. For instance, we find that upper atmospheric positive height anomaly patterns on average are centered over regions with anomalously warm surface temperatures (shading in Fig. 1). In aggregate, droughts appear to be associated with two dominant patterns of surface temperature anomalies: 1) ~20% of droughts cluster in a warm PDO-like pattern (Mantua and Hare 2002), with warm waters off the coast of the North American west coast (top left, Fig. 1), and 2) ~40%–50% of droughts cluster in a cold PDO-like pattern, with cool waters off the North American west coast and particularly warm waters over the Kuroshio Extension region (bottom row, Fig. 1) (McCabe-Glynn et al. 2013; Qiu 2000). Although most droughts coincide with a La Niña-like state (left side, Fig. 2; Seager et al. 2005; Conroy et al. 2009), ~20% of droughts are associated with a cool western tropical Pacific, provided the PDO is in a “cool” state (lower right, Fig. 1). All the CESM LME maps in this SOM (Fig. 1) show a slightly cool tropical Atlantic region (Meehl and Hu 2006) and a warm extratropical North Atlantic region (e.g., McCabe et al. 2004; Seager and Hoerling 2014) south of Greenland. This cool tropical Atlantic relationship with SWNA drought in the CESM LME contrasts with previous research indicating that a warm tropical Atlantic can lead to drought in western North America (e.g., Seager et al. 2005, 2008; Kushnir et al. 2010).

Similar ocean–atmosphere conditions tend to coincide with droughts across a range of time scales as

exhibited by the largely consistent percentage values in Fig. 1 for subdecadal versus decadal drought intervals. Nevertheless, decadal–multidecadal droughts are more likely to coincide with certain atmospheric circulation and surface temperature conditions in the CESM LME. To demonstrate this, we examine the differences between subdecadal and decadal–multidecadal droughts using a random draw approach (see section 2) to determine if each SOM map is statistically more likely to be associated with decadal–multidecadal (versus subdecadal) drought. We find that a cool PDO-like pattern (with positive upper-level geopotential height and positive surface temperature anomalies over the Kuroshio Extension) is significantly more likely to be associated with drought intervals of decadal–multidecadal length (e.g., ~15% of decadal–multidecadal droughts as compared to ~9% of subdecadal droughts; bottom right, Fig. 1). By contrast, subdecadal droughts coincide with a cool eastern tropical Pacific and a weak warm PDO nearly twice as often as decadal–multidecadal droughts (e.g., ~9% of subdecadal droughts vs ~4% of decadal–multidecadal droughts; upper left, Fig. 1). Despite these differences, droughts across time scales coincide with all the patterns shown in Fig. 1, so one length of drought is not exclusively associated with one ocean–atmosphere pattern.

A portion of both subdecadal and decadal–multidecadal droughts (~25%) are associated with geopotential height and SST anomaly patterns of minimal magnitude (top-right panels, Fig. 1). The presence of such weak and/or inconsistent SST patterns during extended drought intervals suggests that consistent SST boundary forcing is not necessary to drive all decadal–multidecadal droughts (e.g., Stevenson et al. 2015), and that these longer droughts can be driven by purely internal atmospheric variability and/or land surface feedbacks.

The SOM methodology allows us to condense large amounts of information about ocean–atmosphere conditions during SWNA droughts into a well-organized map structure, but the SOM methodology has limitations. Specifically, SOMs remove all information about individual drought periods and their dynamics in favor of a single map that represents a composite of these dynamics. Thus, we use a pattern correlation analysis to better understand how consistent the ocean–atmosphere conditions in individual drought periods are with the SOM map to which the drought is assigned. Specifically, the pattern correlation metric is calculated between each individual geopotential height anomaly and TS anomaly pattern and the SOM map to which it was assigned (Fig. 4). Pattern correlations are calculated over the outlined boxes in Figs. 1 and 3 (15°–80°N,

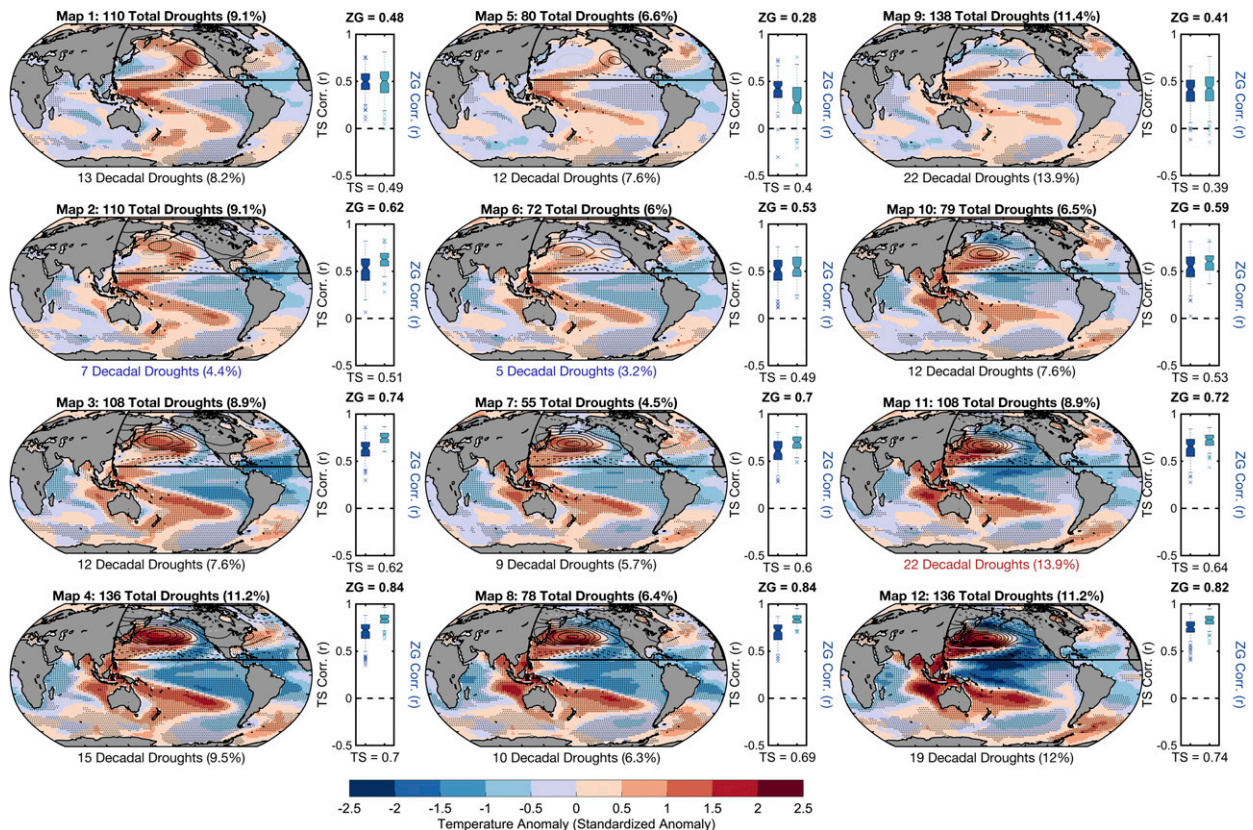


FIG. 4. As in Fig. 1, but panels to the right of each map show the associated distribution of pattern correlations (dark blue boxplots) of individual surface temperature anomaly maps and geopotential height maps (light blue boxplots) within each SOM node. The numbers above (below) each boxplot indicate the mean geopotential height (temperature) correlation in the adjacent boxplots and SOM node.

120°E–360°) for geopotential heights and for TS fields over all ocean regions. The cool “PDO-like” maps (bottom row in Fig. 1; Fig. 4) show the highest internal consistency, with mean pattern correlation values of ~ 0.7 for the TS maps and ~ 0.8 for geopotential height. There is similarly good agreement among the La Niña-like maps (left column in Fig. 4), with median TS and geopotential height R values between ~ 0.5 and 0.8 . The maps associated with weaker surface temperature and upper atmospheric anomaly patterns (upper right, Fig. 4) show less agreement, with median TS R values ranging from 0.39 to 0.6 (and in a few cases, the TS maps within the upper-right map have a negative R value). Disagreement among the TS patterns of the individual droughts with the SOM maps can be interpreted as further evidence that a range of surface temperature patterns can be associated with similar geopotential height anomalies that lead to drought in SWNA. This is particularly true of the upper-right SOM maps in Fig. 4, where the poor agreement in the underlying TS anomaly patterns suggests a large role for stochastic atmospheric variability in driving these droughts. Poor agreement

could also be due to the possibility that multiple ocean–atmosphere states are averaged together during these droughts to create a weak aggregate of anomalies (e.g., Cayan et al. 1998), implying an important role for the trajectory of the ocean–atmosphere conditions and not a persistent state of these conditions. Nevertheless, a PDO-like pattern is the dominant surface boundary condition pattern that coincides with most extended drought in SWNA, and the corresponding SOM maps (bottom row of Fig. 1; Fig. 4) have individual droughts with largely consistent TS boundary conditions.

d. CESM LME–CMIP5 LM SOM comparison

Here we expand our analysis to the nine CMIP5 LM simulations (Table 1) to determine if there is intermodel agreement about the continuum of conditions leading to drought in SWNA. Specifically, in Fig. 5 we show the maximum pattern correlation among each CMIP5 LM 4×3 SOM map with each of the CESM LME SOM maps. The SOM algorithm does not necessarily place similar patterns in the same positions for each of the individual SOM analyses (e.g., the cool PDO-like

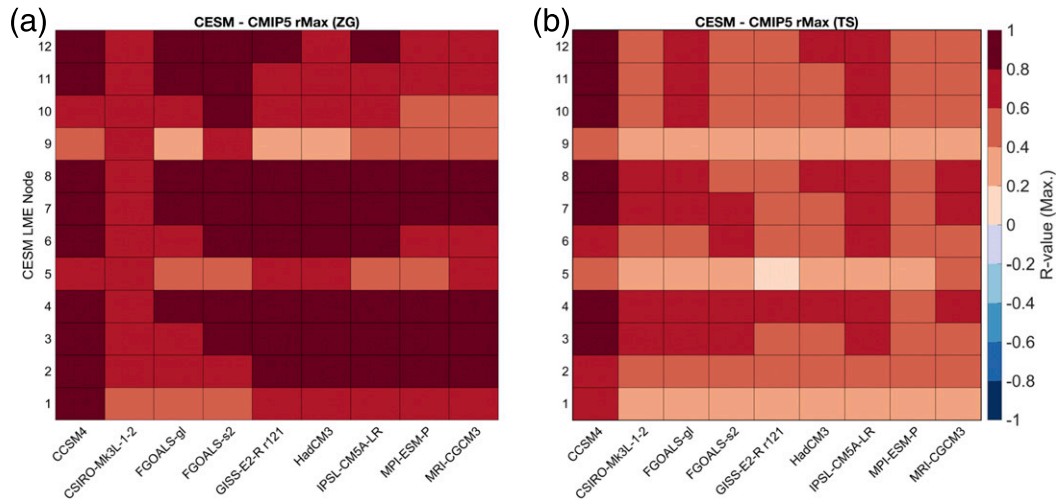


FIG. 5. Heat maps of the maximum pattern correlations (shading) between the 4×3 SOM maps for the CESM LME and the 4×3 SOM maps for the nine CMIP5 LM simulations (using all subdecadal and decadal droughts). (a) Geopotential height pattern correlations over the region outlined in Fig. 1. (b) Surface temperature correlations. Numbers on y axis indicate the CESM LME SOM map (Fig. 1) and its associated maximum pattern correlation across all 12 maps of each CMIP5 LM SOM.

pattern in the lower right in the CESM LME SOM might not be in the lower right for the SOM output from another CMIP5 model). We thus show the maximum pattern correlations between all 12 CMIP5 LM SOM maps and the 12 SOM maps from the CESM LME in two 12×12 correlation matrices, one for geopotential height and one for TS (Fig. 5). There tends to be strong agreement among the CESM and CMIP5 LM simulations that similar ridge-like patterns lead to drought in SWNA (Fig. 5a). NCAR CCSM4, IPSL-CM5A-LR, and FGOALS-s2 tend to show the strongest positive R values, and thus the best agreement with the 250-mb geopotential height SOM maps in the CESM. However, the CSIRO-Mk3L-1.2, FGOALS-G1, HadCM3, and MPI-ESM-P tend to show lower R values with many of the geopotential height patterns in the CESM LME SOM, especially the upper row (e.g., the row with a relatively weak upper-level ridge centered off the west coast of North America).

In general, there is also good agreement among these models that cool PDO-like patterns coincide with strong upper-level ridge patterns over the northwest Pacific. However, these models tend to disagree about the other (noncool PDO) TS patterns that coincide with drought in SWNA (Fig. 5b). Even in the NCAR CCSM4, a model from the same lineage as the CESM, there is relatively poor agreement with the CESM related to TS boundary forcing of SWNA drought for the “warm PDO” drought conditions. The CESM LME and CMIP5 LM SOM map differences likely arise from the differing teleconnection patterns between SWNA and

the Pacific and Atlantic in the different CMIP5 LM models (e.g., Coats et al. 2013a, 2015a), in addition to the differences in the mean state and variability in the Pacific in these models (e.g., Brown et al. 2014; Bellenger et al. 2014).

e. GISS-E2-R LM SOM analysis

Here we use the ensemble of last millennium simulations from the GISS-E2-R model to examine if the relationship between subdecadal versus decadal–multidecadal drought and atmosphere–ocean conditions is similar to the CESM (section 3c; Figs. 1 and 5). This comparison is particularly useful given that the GISS-E2-R model shows a much different mean state (e.g., Brown et al. 2014) and TS variability in the tropical Pacific than the CESM (e.g., Bellenger et al. 2014; Parsons et al. 2017) and is also one of the models with the poorest overall agreement with the CESM SWNA drought patterns (Figs. 5 and 6). Like in the CESM, there are differences in the dynamics of subdecadal versus decadal–multidecadal droughts in the GISS-E2-R, but these differences are manifested mostly as a tropics versus high latitudes zonally symmetric pattern in the GISS-E2-R (Fig. 6). Subdecadal droughts in the GISS-E2-R are significantly more likely (see section 2) to be associated with a La Niña–like cool eastern tropical Pacific and a slightly warm PDO. By contrast, a large proportion ($\sim 35\%$) of decadal–multidecadal droughts are significantly more likely to be associated with a slightly cool PDO-like pattern and a more zonally symmetric TS and geopotential height anomaly pattern

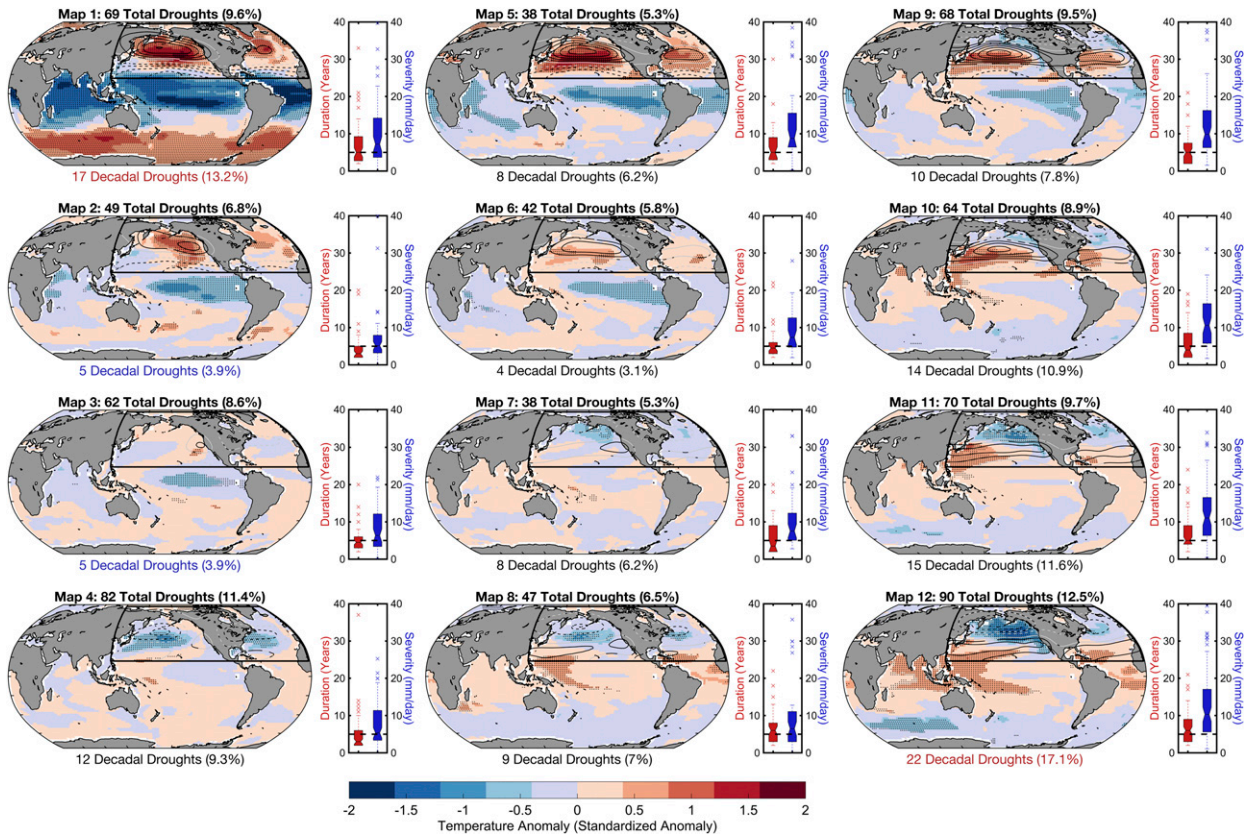


FIG. 6. As in Fig. 1, but for geopotential height (contour lines) and associated surface temperature anomalies (shading) from nine NASA GISS-E2-R LM (past1000) simulations during droughts ($N = 715$ composite climate states during drought in this SOM, ranging in length from 2 to 33 years, including 147 decadal–multidecadal droughts).

(bottom right maps, Fig. 6). The zonal TS anomaly differences manifest themselves in the atmosphere as well; droughts in the GISS-E2-R tend to be associated with strong zonally symmetric geopotential height patterns at $\sim 40^{\circ}$ – 50° N (top row, Fig. 6) and at $\sim 30^{\circ}$ – 40° N (bottom row, Fig. 6). This zonal tropical versus extratropical pattern may partly be attributed to the simulated effects of volcanic forcing in the GISS-E2-R, in which aerosols from volcanic eruptions appear to show a similar zonal impact (e.g., Driscoll et al. 2012; Parsons et al. 2017). It is important to note that each of these nine GISS simulations uses different combinations of forcings over the last millennium (Schmidt et al. 2012), making the comparison to the CESM results imperfect (as the 12 CESM LME simulations have the same forcings as each other and different forcings than the nine GISS simulations).

4. Conclusions

Here we examine the continuum of SWNA drought lengths in instrumental, paleoclimate, and CMIP5-class model data. We find that the overall distribution and continuum of simulated drought lengths appears

consistent with the paleoclimate-based NADAv2a drought reconstruction (Stevenson et al. 2017; Coats et al. 2015b). The CESM LME, GISS-E2-R LM, CMIP5 LM, and NADAv2a data tend to agree that the region experiences distinct droughts lasting two to three years multiple times per century, droughts last lasting five years about once per century, droughts spanning 5–10 years about once every other century, and a decadal-scale drought once every few centuries (Fig. 3). However, the mean CESM LME and CMIP5 LM simulations may overestimate the risk of short droughts (<5 yr) and underestimate the risk of longer droughts (15–20 yr) as compared to the NADAv2a. These findings confirm recent work that suggests a discrepancy in low-frequency hydroclimatic variability between observations, climate models and the paleoclimate record (e.g., Ault et al. 2013; Coats et al. 2015b; Stevenson et al. 2015; Otto-Bliesner et al. 2016). Although proxy records may present spectral biases that project onto climate reconstructions (e.g., Franke et al. 2013), the NADAv2a has relatively consistent and widespread data coverage over SWNA in the last millennium and should capture SWNA drought timing (based on instrumental-era

verification; e.g., Cook et al. 2010). However, since we rely solely on the NADAv2a for verifying if the latest climate models are able to reproduce the real-world SWNA drought length continuum, it is difficult to determine if these differences result from model bias. Nonetheless, the NADAv2a is currently one of the only publicly available, annually resolved, observationally based data sources for studying annually resolved hydroclimatic variability of the past in North America and represents an important benchmark for model simulations.

Despite these CMIP5-NADAv2a data discrepancies, these data sources agree that SWNA has experienced multidecadal droughts multiple times over the last millennium. However, there is a limited understanding of the drivers of SWNA drought across the range of time scales on which it occurs. Here we attempt to answer if droughts from interannual-to-multidecadal time scales are associated with similar ocean–atmosphere conditions. Using a SOM analysis we find that droughts of all lengths coincide with atmospheric “ridges” (positive geopotential height anomalies) at 250 mb over the North Pacific. The atmospheric conditions leading to drought are similar across time scales, and at least half of decadal–multidecadal SWNA droughts in the CESM LME are also associated with pronounced surface temperature boundary conditions, predominantly manifesting as a cool tropical Pacific, cold PDO-like extratropical Pacific, warm extratropical North Atlantic, and cool tropical North Atlantic. Although these conditions appear increasingly important for longer droughts, many droughts lasting decades can occur with relatively weak or inconsistent SST boundary forcing, supporting the idea that extended SWNA dry periods can arise from purely atmospheric forcing in climate models (e.g., Coats et al. 2013b, 2015b; Stevenson et al. 2015).

Cold PDO-like conditions appear to consistently coincide with certain patterns of 250-mb geopotential height anomalies over the extratropical Pacific (Fig. 1), but we have not shown that these SST anomalies are driving atmospheric variability, nor have we shown if persistent atmospheric forcing is driving variability at the ocean surface (e.g., Davis 1976; Trenberth and Hurrell 1994; Deser et al. 1999; Schneider and Cornuelle 2005). Nevertheless, there is a clearer relationship between tropical Pacific SSTs and extratropical atmospheric circulation that suggests changes in the tropical Pacific Ocean tend to lead extratropical Pacific atmospheric circulation changes (e.g., Schneider and Cornuelle 2005; Trenberth and Hurrell 1994).

The SOM analysis additionally shows that many CMIP5 LM models simulate similar ocean–atmosphere patterns to the CESM LME during SWNA drought:

positive 250-mb atmospheric pressure anomalies (e.g., ridges) coincide with droughts in SWNA on interannual–multidecadal time scales. Likewise, these atmospheric ridge patterns tend to be associated with a cool PDO-like pattern and a cool tropical North Atlantic, particularly for droughts of decadal–multidecadal length. Despite the relatively similar SWNA PR teleconnection patterns in most CMIP5 models (with SST and geopotential height fields; e.g., Fig. 2), the SOM analysis reveals that the ocean–atmosphere conditions associated with SWNA drought can be different across models. Specifically, the GISS-E2-R suggests decadal–multidecadal droughts tend to coincide with a more zonally symmetric high pressure pattern extending from the Pacific to the Atlantic and that a warm North Atlantic can drive extended dry periods in SWNA. This pattern is not consistent with the more zonally asymmetric “wave train” that originates via changes in convection in the tropical Pacific in many models and observations and that tends to dominate the coupled variability of the tropical Pacific and extratropical atmosphere (e.g., Trenberth et al. 1998; Seager et al. 2003). Agreement among CMIP5 LM models in terms of their SWNA drought dynamics may be related, in part, to each model’s representation of the mean state and variability in the tropical Pacific. A better understanding and simulation of the tropical Pacific is critical to provide confidence in the ability of CMIP5-class models to simulate the dynamics of SWNA drought across time scales.

Even though the tropical Pacific teleconnection to hydroclimate in SWNA is stronger in the CESM than in observations (and thus likely stronger than in the real world; e.g., Fig. 2), there is still an important role for purely atmospheric forcing in driving extended drought in SWNA. This role in the real world thus might be expected to be even larger than in the CESM. However, the tropical Atlantic appears to play a consistently weak role in driving SWNA drought in the CESM, and CMIP5-class models tend to struggle to reproduce observed teleconnections between North American hydroclimate and the Atlantic (McCabe et al. 2004; Ting et al. 2009; Conroy et al. 2009; Kushnir et al. 2010; Coats et al. 2015a). The North Atlantic is a region that has large magnitude decadal–multidecadal time scale variability, so these models may also be underestimating the role of oceanic forcing of drought in SWNA.

Our analysis shows the utility of the SOM framework for studying the continuum of climate variability across time scales. These findings advance our understanding of extended, potentially catastrophic drought. As we (and others; e.g., Coats et al. 2015b) have shown, there is an inconsistent relationship between the SST boundary conditions and extended droughts in SWNA. While

there appears to be a continuum of conditions that lead to extended droughts, with a variety of persistent surface temperature boundary conditions in the Pacific (and Atlantic) leading to drought across time scales, internal atmospheric variability can also lead to a significant portion of decadal-to-multidecadal droughts. These findings are important for the predictability of “megadrought” events (e.g., Karspeck et al. 2004; Seager et al. 2004), as a role for stochastic atmospheric variability in driving these features implies limited potential predictability. Furthermore, these results highlight the importance of improving model simulations; CMIP5-class models generate drought in SWNA region via a combination of internal atmospheric variability, SST forcing, external forcing, and local land–atmosphere feedbacks, all of which must be realistically simulated (e.g., Langford et al. 2014; Cook et al. 2016). Recent work has highlighted the need to improve simulated Pacific variability (e.g., Cheung et al. 2017; Parsons et al. 2017), Atlantic teleconnections (e.g., Coats et al. 2015a,b; Ting et al. 2009; Kushnir et al. 2010), and local land–atmosphere feedbacks (e.g., Langford et al. 2014). We also need to advance our understanding of how anthropogenic forcing may impact Pacific surface temperature variability and persistence in the twenty-first century as this region plays an important role in driving drought across time scales and intermodel differences in the dynamics of such droughts.

Acknowledgments. The National Science Foundation EaSM2 Grant (AGS1243125) supported this work. We thank D. Reusch for valuable feedback related to the SOM analysis and B. Otto-Bliesner at NCAR for providing the CESM Last Millennium Ensemble data. We acknowledge the World Climate Research Program’s Working Group on Coupled Modeling, which is responsible for CMIP, and we thank the climate modeling groups for producing and making available their model output. For CMIP the U.S. Department of Energy’s Program for Climate Model Diagnosis and Intercomparison provides coordinating support and led development of software infrastructure in partnership with the Global Organization for Earth System Science Portals. Dai Palmer drought severity index and other gridded instrumental-based data provided by the NOAA/OAR/ESRL PSD, Boulder, Colorado, from their website at <http://www.esrl.noaa.gov/psd/>.

REFERENCES

- Acuna-Soto, R., D. W. Stahle, M. K. Cleaveland, and M. D. Therrell, 2002: Megadrought and megadeath in 16th century Mexico. *Emerging Infect. Dis.*, **8**, 360–362, <https://doi.org/10.3201/eid0804.010175>.
- Ault, T. R., J. E. Cole, J. T. Overpeck, G. T. Pederson, S. St. George, B. Otto-Bliesner, C. A. Woodhouse, and C. Deser, 2013: The continuum of hydroclimate variability in western North America during the last millennium. *J. Climate*, **26**, 5863–5878, <https://doi.org/10.1175/JCLI-D-11-00732.1>.
- , —, —, —, and D. M. Meko, 2014: Assessing the risk of persistent drought using climate model simulations and paleoclimate data. *J. Climate*, **27**, 7529–7549, <https://doi.org/10.1175/JCLI-D-12-00282.1>.
- , J. S. Mankin, B. I. Cook, and J. E. Smerdon, 2016: Relative impacts of mitigation, temperature, and precipitation on 21st-century megadrought risk in the American Southwest. *Sci. Adv.*, **2**, e1600873, <https://doi.org/10.1126/sciadv.1600873>.
- , S. St. George, J. E. Smerdon, S. Coats, J. S. Mankin, C. M. Carrillo, B. I. Cook, and S. Stevenson, 2018: A robust null hypothesis for the potential causes of megadrought in western North America. *J. Climate*, **31**, 3–24, <https://doi.org/10.1175/JCLI-D-17-0154.1>.
- Bellenger, H., E. Guilyardi, J. Leloup, M. Lengaigne, and J. Vialard, 2014: ENSO representation in climate models: From CMIP3 to CMIP5. *Climate Dyn.*, **42**, 1999–2018, <https://doi.org/10.1007/s00382-013-1783-z>.
- Berg, A., and Coauthors, 2016: Land–atmosphere feedbacks amplify aridity increase over land under global warming. *Nat. Climate Change*, **6**, 869–874, <https://doi.org/10.1038/nclimate3029>.
- Bjerknes, J., 1969: Atmospheric teleconnections from the equatorial Pacific. *Mon. Wea. Rev.*, **97**, 163–172, [https://doi.org/10.1175/1520-0493\(1969\)097<0163:ATFTEP>2.3.CO;2](https://doi.org/10.1175/1520-0493(1969)097<0163:ATFTEP>2.3.CO;2).
- Brown, J. N., C. Langlais, and C. Maes, 2014: Zonal structure and variability of the western Pacific dynamic warm pool edge in CMIP5. *Climate Dyn.*, **42**, 3061–3076, <https://doi.org/10.1007/s00382-013-1931-5>.
- Cassano, J. J., P. Uotila, A. H. Lynch, and E. N. Cassano, 2007: Predicted changes in synoptic forcing of net precipitation in large Arctic river basins during the 21st century. *J. Geophys. Res. Biogeosci.*, **112**, G04S49, <https://doi.org/10.1029/2006JG000332>.
- Cavazos, T., 2000: Using self-organizing maps to investigate extreme climate events: An application to wintertime precipitation in the Balkans. *J. Climate*, **13**, 1718–1732, [https://doi.org/10.1175/1520-0442\(2000\)013<1718:USOMTI>2.0.CO;2](https://doi.org/10.1175/1520-0442(2000)013<1718:USOMTI>2.0.CO;2).
- , A. C. Comrie, and D. M. Liverman, 2002: Intraseasonal variability associated with wet monsoons in southeast Arizona. *J. Climate*, **15**, 2477–2490, [https://doi.org/10.1175/1520-0442\(2002\)015<2477:IVAWWM>2.0.CO;2](https://doi.org/10.1175/1520-0442(2002)015<2477:IVAWWM>2.0.CO;2).
- Cayan, D. R., and D. H. Peterson, 1989: The influence of North Pacific atmospheric circulation on streamflow in the west. Aspects of *Climate Variability* in the Pacific and the Western Americas, *Geophys. Monogr.*, Vol. 55, Amer. Geophys. Union, 375–397.
- , M. D. Dettinger, H. F. Diaz, and N. E. Graham, 1998: Decadal variability of precipitation over western North America. *J. Climate*, **11**, 3148–3166, [https://doi.org/10.1175/1520-0442\(1998\)011<3148:DVOPOW>2.0.CO;2](https://doi.org/10.1175/1520-0442(1998)011<3148:DVOPOW>2.0.CO;2).
- , K. T. Redmond, and L. G. Riddle, 1999: ENSO and hydrologic extremes in the western United States. *J. Climate*, **12**, 2881–2893, [https://doi.org/10.1175/1520-0442\(1999\)012<2881:EAHEIT>2.0.CO;2](https://doi.org/10.1175/1520-0442(1999)012<2881:EAHEIT>2.0.CO;2).
- Cheung, A. H., M. E. Mann, B. A. Steinman, L. M. Frankcombe, M. H. England, and S. K. Miller, 2017: Comparison of low-frequency internal climate variability in CMIP5 models and observations. *J. Climate*, **30**, 4763–4776, <https://doi.org/10.1175/JCLI-D-16-0712.1>.

- Coats, S., J. E. Smerdon, B. I. Cook, and R. Seager, 2013a: Stationarity of the tropical Pacific teleconnection to North America in CMIP5/PMIP3 model simulations. *Geophys. Res. Lett.*, **40**, 4927–4932, <https://doi.org/10.1002/grl.50938>.
- , —, R. Seager, B. I. Cook, and J. F. González-Rouco, 2013b: Megadroughts in southwestern North America in ECHO-G millennial simulations and their comparison to proxy drought reconstructions. *J. Climate*, **26**, 7635–7649, <https://doi.org/10.1175/JCLI-D-12-00603.1>.
- , B. I. Cook, J. E. Smerdon, and R. Seager, 2015a: North American noncontinental droughts in model simulations of the last millennium. *J. Climate*, **28**, 2025–2043, <https://doi.org/10.1175/JCLI-D-14-00634.1>.
- , J. E. Smerdon, B. I. Cook, and R. Seager, 2015b: Are simulated megadroughts in the North American Southwest forced? *J. Climate*, **28**, 124–142, <https://doi.org/10.1175/JCLI-D-14-00071.1>.
- , —, R. Seager, D. Griffin, and B. I. Cook, 2015c: Winter-to-summer precipitation phasing in southwestern North America: A multicentury perspective from paleoclimatic model–data comparisons. *J. Geophys. Res. Atmos.*, **120**, 8052–8064, <https://doi.org/10.1002/2015JD023085>.
- , —, B. I. Cook, R. Seager, E. R. Cook, and K. J. Anchukaitis, 2016a: Internal ocean–atmosphere variability drives megadroughts in western North America. *Geophys. Res. Lett.*, **43**, 9886–9894, <https://doi.org/10.1002/2016GL070105>.
- , —, K. B. Karnauskas, and R. Seager, 2016b: The improbable but unexceptional occurrence of megadrought clustering in the American West during the Medieval Climate Anomaly. *Environ. Res. Lett.*, **11**, 074025, <https://doi.org/10.1088/1748-9326/11/7/074025>.
- Cole, J. E., J. T. Overpeck, and E. R. Cook, 2002: Multiyear La Niña events and persistent drought in the contiguous United States. *Geophys. Res. Lett.*, **29**, 1647, <https://doi.org/10.1029/2001GL013561>.
- Compo, G. P., and Coauthors, 2011: The Twentieth Century Reanalysis Project. *Quart. J. Roy. Meteor. Soc.*, **137**, 1–28, <https://doi.org/10.1002/qj.776>.
- Conroy, J. L., J. T. Overpeck, J. E. Cole, and M. Steinitz-Kannan, 2009: Variable oceanic influences on western North American drought over the last 1200 years. *Geophys. Res. Lett.*, **36**, L17703, <https://doi.org/10.1029/2009GL039558>.
- Cook, B. I., J. E. Smerdon, R. Seager, and E. R. Cook, 2014: Pan-continental droughts in North America over the last millennium. *J. Climate*, **27**, 383–397, <https://doi.org/10.1175/JCLI-D-13-00100.1>.
- , T. R. Ault, and J. E. Smerdon, 2015: Unprecedented 21st century drought risk in the American Southwest and central plains. *Sci. Adv.*, **1**, e1400082, <https://doi.org/10.1126/sciadv.1400082>.
- , E. R. Cook, J. E. Smerdon, R. Seager, A. P. Williams, S. Coats, D. W. Stahle, and J. Villanueva Díaz, 2016: North American megadroughts in the Common Era: Reconstructions and simulations. *Wiley Interdiscip. Rev.: Climate Change*, **7**, 411–432, <https://doi.org/10.1002/wcc.394>.
- Cook, E. R., C. A. Woodhouse, C. M. Eakin, D. M. Meko, and D. W. Stahle, 2004: Long-term aridity changes in the western United States. *Science*, **306**, 1015–1018, <https://doi.org/10.1126/science.1102586>.
- , R. Seager, M. A. Cane, and D. W. Stahle, 2007: North American drought: Reconstructions, causes, and consequences. *Earth-Sci. Rev.*, **81**, 93–134, <https://doi.org/10.1016/j.earscirev.2006.12.002>.
- , U. Lall, and C. Woodhouse, 2008: North American summer PDSI reconstructions, version 2a. IGBP PAGES/World Data Center for Paleoclimatology Data Contribution Series 2008-046, accessed June 2015, <http://iridl.ldeo.columbia.edu/SOURCES/LDEO/TRL/NADAv2a-2008/datasetdatafiles.html>.
- , R. Seager, R. R. Heim, R. S. Vose, C. Herweijer, and C. Woodhouse, 2010: Megadroughts in North America: Placing IPCC projections of hydroclimatic change in a long-term palaeoclimate context. *J. Quat. Sci.*, **25**, 48–61, <https://doi.org/10.1002/jqs.1303>.
- Dai, A., 2013: Increasing drought under global warming in observations and models. *Nat. Climate Change*, **3**, 52–58, <https://doi.org/10.1038/nclimate1633>.
- , K. E. Trenberth, and T. Qian, 2004: A global dataset of Palmer Drought Severity Index for 1870–2002: Relationship with soil moisture and effects of surface warming. *J. Hydrometeorol.*, **5**, 1117–1130, <https://doi.org/10.1175/JHM-386.1>.
- Davis, R. E., 1976: Predictability of sea surface temperature and sea level pressure anomalies over the North Pacific Ocean. *J. Phys. Oceanogr.*, **6**, 249–266, [https://doi.org/10.1175/1520-0485\(1976\)006<0249:POSSTA>2.0.CO;2](https://doi.org/10.1175/1520-0485(1976)006<0249:POSSTA>2.0.CO;2).
- Delworth, T., and S. Manabe, 1989: The influence of soil wetness on near-surface atmospheric variability. *J. Climate*, **2**, 1447–1462, [https://doi.org/10.1175/1520-0442\(1989\)002<1447:TIOSWO>2.0.CO;2](https://doi.org/10.1175/1520-0442(1989)002<1447:TIOSWO>2.0.CO;2).
- Deser, C., M. A. Alexander, and M. S. Timlin, 1999: Evidence for a wind-driven intensification of the Kuroshio Current Extension from the 1970s to the 1980s. *J. Climate*, **12**, 1697–1706, [https://doi.org/10.1175/1520-0442\(1999\)012<1697:EFAWDI>2.0.CO;2](https://doi.org/10.1175/1520-0442(1999)012<1697:EFAWDI>2.0.CO;2).
- Dettinger, M. D., D. R. Cayan, H. F. Diaz, and D. M. Meko, 1998: North–south precipitation patterns in western North America on interannual-to-decadal timescales. *J. Climate*, **11**, 3095–3111, [https://doi.org/10.1175/1520-0442\(1998\)011<3095:NSPPIW>2.0.CO;2](https://doi.org/10.1175/1520-0442(1998)011<3095:NSPPIW>2.0.CO;2).
- Diffenbaugh, N. S., D. L. Swain, and D. Touma, 2015: Anthropogenic warming has increased drought risk in California. *Proc. Natl. Acad. Sci. USA*, **112**, 3931–3936, <https://doi.org/10.1073/pnas.1422385112>.
- Driscoll, S., A. Bozzo, L. J. Gray, A. Robock, and G. Stenchikov, 2012: Coupled Model Intercomparison Project 5 (CMIP5) simulations of climate following volcanic eruptions. *J. Geophys. Res.*, **117**, D17105, <https://doi.org/10.1029/2012JD017607>.
- Flato, G., and Coauthors, 2013: Evaluation of climate models. *Climate Change 2013: The Physical Science Basis*, T. F. Stocker et al., Eds., Cambridge University Press, 741–866.
- Franke, J., D. Frank, C. C. Raible, J. Esper, and S. Brönnimann, 2013: Spectral biases in tree-ring climate proxies. *Nat. Climate Change*, **3**, 360–364, <https://doi.org/10.1038/nclimate1816>.
- Gibson, P. B., S. E. Perkins-Kirkpatrick, P. Uotila, A. S. Pepler, and L. V. Alexander, 2017: On the use of self-organizing maps for studying climate extremes. *J. Geophys. Res. Atmos.*, **122**, 3891–3903, <https://doi.org/10.1002/2016JD026256>.
- Green, J., 1977: The weather during July 1976: Some dynamical considerations of the drought. *Weather*, **32**, 120–126, <https://doi.org/10.1002/j.1477-8696.1977.tb04532.x>.
- Gutzler, D. S., and J. W. Preston, 1997: Evidence for a relationship between spring snow cover in North America and summer rainfall in New Mexico. *Geophys. Res. Lett.*, **24**, 2207–2210, <https://doi.org/10.1029/97GL02099>.
- Herweijer, C., R. Seager, E. R. Cook, and J. Emile-Geay, 2007: North American droughts of the last millennium from a gridded network of tree-ring data. *J. Climate*, **20**, 1353–1376, <https://doi.org/10.1175/JCLI4042.1>.

- Hewitson, B., and R. Crane, 2002: Self-organizing maps: Applications to synoptic climatology. *Climate Res.*, **22**, 13–26, <https://doi.org/10.3354/cr022013>.
- Jacobi, J., D. Perrone, L. L. Duncan, and G. Hornberger, 2013: A tool for calculating the Palmer drought indices. *Water Resour. Res.*, **49**, 6086–6089, <https://doi.org/10.1002/wrcr.20342>.
- Johnson, N. C., S. B. Feldstein, and B. Tremblay, 2008: The continuum of Northern Hemisphere teleconnection patterns and a description of the NAO shift with the use of self-organizing maps. *J. Climate*, **21**, 6354–6371, <https://doi.org/10.1175/2008JCLI2380.1>.
- Karspeck, A. R., R. Seager, and M. A. Cane, 2004: Predictability of tropical Pacific decadal variability in an intermediate model. *J. Climate*, **17**, 2842–2850, [https://doi.org/10.1175/1520-0442\(2004\)017<2842:POTPDV>2.0.CO;2](https://doi.org/10.1175/1520-0442(2004)017<2842:POTPDV>2.0.CO;2).
- Kohonen, T., 1982: Self-organizing formation of topologically correct map features. *Biol. Cybern.*, **43**, 59–69, <https://doi.org/10.1007/BF00337288>.
- Kushnir, Y., R. Seager, M. Ting, N. Naik, and J. Nakamura, 2010: Mechanisms of tropical Atlantic SST influence on North American precipitation variability. *J. Climate*, **23**, 5610–5628, <https://doi.org/10.1175/2010JCLI3172.1>.
- Langford, S., S. Stevenson, and D. Noone, 2014: Analysis of low-frequency precipitation variability in CMIP5 historical simulations for southwestern North America. *J. Climate*, **27**, 2735–2756, <https://doi.org/10.1175/JCLI-D-13-00317.1>.
- Latif, M., and T. P. Barnett, 1994: Causes of decadal climate variability over the North Pacific and North America. *Science*, **266**, 634–638, <https://doi.org/10.1126/science.266.5185.634>.
- Liu, Y., R. H. Weisberg, and C. N. Mooers, 2006: Performance evaluation of the self-organizing map for feature extraction. *J. Geophys. Res.*, **111**, C05018, <https://doi.org/10.1029/2005JC003117>.
- Mantua, N. J., and S. R. Hare, 2002: The Pacific decadal oscillation. *J. Oceanogr.*, **58**, 35–44, <https://doi.org/10.1023/A:1015820616384>.
- McCabe, G. J., and M. D. Dettinger, 1999: Decadal variations in the strength of ENSO teleconnections with precipitation in the western United States. *Int. J. Climatol.*, **19**, 1399–1410, [https://doi.org/10.1002/\(SICI\)1097-0088\(19991115\)19:13<1399::AID-JOC457>3.0.CO;2-A](https://doi.org/10.1002/(SICI)1097-0088(19991115)19:13<1399::AID-JOC457>3.0.CO;2-A).
- , M. A. Palecki, and J. L. Betancourt, 2004: Pacific and Atlantic Ocean influences on multidecadal drought frequency in the United States. *Proc. Natl. Acad. Sci. USA*, **101**, 4136–4141, <https://doi.org/10.1073/pnas.0306738101>.
- McCabe-Glynn, S., K. R. Johnson, C. Strong, M. Berkelhammer, A. Sinha, H. Cheng, and R. L. Edwards, 2013: Variable North Pacific influence on drought in southwestern North America since AD 854. *Nat. Geosci.*, **6**, 617–621, <https://doi.org/10.1038/ngeo1862>.
- Meehl, J., and A. Hu, 2006: Megadroughts in the Indian monsoon region and southwest North America and a mechanism for associated multidecadal Pacific sea surface temperature anomalies. *J. Climate*, **19**, 1605–1623, <https://doi.org/10.1175/JCLI3675.1>.
- Milly, P. C., and K. A. Dunne, 2016: Potential evapotranspiration and continental drying. *Nat. Climate Change*, **6**, 946–949, <https://doi.org/10.1038/nclimate3046>.
- Otto-Bliessner, B., and Coauthors, 2016: Climate variability and change since 850 C.E.: An ensemble approach with the Community Earth System Model (CESM). *Bull. Amer. Meteor. Soc.*, **97**, 735–754, <https://doi.org/10.1175/BAMS-D-14-00233.1>.
- Palmer, W. C., 1965: Meteorological drought. Weather Bureau Res. Paper 45, U.S. Department of Commerce, 58 pp.
- Parsons, L. A., G. R. Loope, J. T. Overpeck, T. R. Ault, R. Stouffer, and J. E. Cole, 2017: Temperature and precipitation variance in CMIP5 simulations and paleoclimate records of the last millennium. *J. Climate*, **30**, 8885–8912, <https://doi.org/10.1175/JCLI-D-16-0863.1>.
- Qiu, B., 2000: Interannual variability of the Kuroshio Extension system and its impact on the wintertime SST field. *J. Phys. Oceanogr.*, **30**, 1486–1502, [https://doi.org/10.1175/1520-0485\(2000\)030<1486:IVOTKE>2.0.CO;2](https://doi.org/10.1175/1520-0485(2000)030<1486:IVOTKE>2.0.CO;2).
- Rayner, N., D. Parker, E. Horton, C. Folland, L. Alexander, D. Rowell, E. Kent, and A. Kaplan, 2003: Global analyses of sea surface temperature, sea ice, and night marine air temperature since the late nineteenth century. *J. Geophys. Res.*, **108**, 4407, <https://doi.org/10.1029/2002JD002670>.
- Reusch, D. B., R. B. Alley, and B. C. Hewitson, 2005: Relative performance of self-organizing maps and principal component analysis in pattern extraction from synthetic climatological data. *Polar Geogr.*, **29**, 188–212, <https://doi.org/10.1080/789610199>.
- , —, and —, 2007: North Atlantic climate variability from a self-organizing map perspective. *J. Geophys. Res.*, **112**, D02104, <https://doi.org/10.1029/2006JD007460>.
- Roderick, M. L., P. Greve, and G. D. Farquhar, 2015: On the assessment of aridity with changes in atmospheric CO₂. *Water Resour. Res.*, **51**, 5450–5463, <https://doi.org/10.1002/2015WR017031>.
- Routson, C. C., C. A. Woodhouse, J. T. Overpeck, J. L. Betancourt, and N. P. McKay, 2016: Teleconnected ocean forcing of western North American droughts and pluvials during the last millennium. *Quat. Sci. Rev.*, **146**, 238–250, <https://doi.org/10.1016/j.quascirev.2016.06.017>.
- Scheff, J., R. Seager, H. Liu, and S. Coats, 2017: Are glacials dry? Consequences for paleoclimatology and for greenhouse warming. *J. Climate*, **30**, 6593–6609, <https://doi.org/10.1175/JCLI-D-16-0854.1>.
- Schmidt, G. A., and Coauthors, 2012: Climate forcing reconstructions for use in PMIP simulations of the Last Millennium (v1.1). *Geosci. Model Dev.*, **5**, 185–191, <https://doi.org/10.5194/gmd-5-185-2012>.
- , and Coauthors, 2014: Configuration and assessment of the GISS ModelE2 contributions to the CMIP5 archive. *J. Adv. Model. Earth Syst.*, **6**, 141–184, <https://doi.org/10.1002/2013MS000265>.
- Schneider, N., and B. D. Cornuelle, 2005: The forcing of the Pacific decadal oscillation. *J. Climate*, **18**, 4355–4373, <https://doi.org/10.1175/JCLI3527.1>.
- Schneider, U., A. Becker, P. Finger, A. Meyer-Christoffer, M. Ziese, and B. Rudolf, 2014: GPCC's new land surface precipitation climatology based on quality-controlled in situ data and its role in quantifying the global water cycle. *Theor. Appl. Climatol.*, **115**, 15–40, <https://doi.org/10.1007/s00704-013-0860-x>.
- Seager, R., 2007: The turn of the century North American drought: Global context, dynamics, and past analogs. *J. Climate*, **20**, 5527–5552, <https://doi.org/10.1175/2007JCLI1529.1>.
- , and M. Hoerling, 2014: Atmosphere and ocean origins of North American droughts. *J. Climate*, **27**, 4581–4606, <https://doi.org/10.1175/JCLI-D-13-00329.1>.
- , R. Murtugudde, N. Naik, A. Clement, N. Gordon, and J. Miller, 2003: Air–sea interaction and the seasonal cycle of the subtropical anticyclones. *J. Climate*, **16**, 1948–1966, [https://doi.org/10.1175/1520-0442\(2003\)016<1948:AIATSC>2.0.CO;2](https://doi.org/10.1175/1520-0442(2003)016<1948:AIATSC>2.0.CO;2).
- , A. R. Karspeck, M. A. Cane, Y. Kushnir, A. Giannini, A. Kaplan, B. Kerman, and J. Velez, 2004: Predicting Pacific

- decadal variability. *Earth's Climate: The Ocean–Atmosphere Interaction, Geophys. Monogr.*, Vol. 147, Amer. Geophys. Union, 105–120, <https://doi.org/10.1029/147GM06>.
- , Y. Kushnir, C. Herweijer, N. Naik, and J. Velez, 2005: Modeling of tropical forcing of persistent droughts and pluvials over western North America: 1856–2000. *J. Climate*, **18**, 4065–4088, <https://doi.org/10.1175/JCLI3522.1>.
- , R. Burgman, Y. Kushnir, A. Clement, E. Cook, N. Naik, and J. Miller, 2008: Tropical Pacific forcing of North American medieval megadroughts: Testing the concept with an atmosphere model forced by coral-reconstructed SSTs. *J. Climate*, **21**, 6175–6190, <https://doi.org/10.1175/2008JCLI2170.1>.
- , M. Hoerling, S. Schubert, H. Wang, B. Lyon, A. Kumar, J. Nakamura, and N. Henderson, 2015: Causes of the 2011–14 California drought. *J. Climate*, **28**, 6997–7024, <https://doi.org/10.1175/JCLI-D-14-00860.1>.
- Stahle, D. W., F. K. Fye, E. R. Cook, and R. D. Griffin, 2007: Tree-ring reconstructed megadroughts over North America since AD 1300. *Climatic Change*, **83**, 133–149, <https://doi.org/10.1007/s10584-006-9171-x>.
- Stevenson, S., A. Timmermann, Y. Chikamoto, S. Langford, and P. DiNezio, 2015: Stochastically generated North American megadroughts. *J. Climate*, **28**, 1865–1880, <https://doi.org/10.1175/JCLI-D-13-00689.1>.
- , B. Otto-Bliesner, J. Fasullo, and E. Brady, 2016: “El Niño like” hydroclimate responses to last millennium volcanic eruptions. *J. Climate*, **29**, 2907–2921, <https://doi.org/10.1175/JCLI-D-15-0239.1>.
- , J. T. Fasullo, B. L. Otto-Bliesner, R. A. Tomas, and C. Gao, 2017: Role of eruption season in reconciling model and proxy responses to tropical volcanism. *Proc. Natl. Acad. Sci. USA*, **114**, 1822–1826, <https://doi.org/10.1073/pnas.1612505114>.
- , and Coauthors, 2018: Climate variability, volcanic forcing, and last millennium hydroclimate extremes. *J. Climate*, **31**, 4309–4327, <https://doi.org/10.1175/JCLI-D-17-0407.1>.
- Swain, D. L., 2015: A tale of two California droughts: Lessons amidst record warmth and dryness in a region of complex physical and human geography. *Geophys. Res. Lett.*, **42**, 9999–10 003, <https://doi.org/10.1002/2015GL066628>.
- , M. Tsiang, M. Haugen, D. Singh, A. Charland, B. Rajaratnam, and N. S. Diffenbaugh, 2014: The extraordinary California drought of 2013/2014: Character, context, and the role of climate change [in “Explaining Extremes of 2013 from a Climate Perspective”]. *Bull. Amer. Meteor. Soc.*, **95** (9), S3–S7, <https://doi.org/10.1175/1520-0477-95.9.S1.1>.
- Taylor, K. E., R. J. Stouffer, and G. A. Meehl, 2012: An overview of CMIP5 and the experiment design. *Bull. Amer. Meteor. Soc.*, **93**, 485–498, <https://doi.org/10.1175/BAMS-D-11-00094.1>.
- Ting, M., Y. Kushnir, R. Seager, and C. Li, 2009: Forced and internal twentieth-century SST trends in the North Atlantic. *J. Climate*, **22**, 1469–1481, <https://doi.org/10.1175/2008JCLI2561.1>.
- Trenberth, K. E., and J. W. Hurrell, 1994: Decadal atmosphere–ocean variations in the Pacific. *Climate Dyn.*, **9**, 303–319, <https://doi.org/10.1007/BF00204745>.
- , G. W. Branstator, and P. A. Arkin, 1988: Origins of the 1988 North American drought. *Science*, **242**, 1640–1645, <https://doi.org/10.1126/science.242.4886.1640>.
- , —, D. Karoly, A. Kumar, N.-C. Lau, and C. Ropelewski, 1998: Progress during TOGA in understanding and modeling global teleconnections associated with tropical sea surface temperatures. *J. Geophys. Res. Oceans*, **103**, 14291–14324, <https://doi.org/10.1029/97JC01444>.
- Udall, B., and J. Overpeck, 2017: The twenty-first century Colorado River hot drought and implications for the future. *Water Resour. Res.*, **53**, 2404–2418, <https://doi.org/10.1002/2016WR019638>.
- Wang, S., L. Hippias, R. R. Gillies, and J. Yoon, 2014: Probable causes of the abnormal ridge accompanying the 2013–2014 California drought: ENSO precursor and anthropogenic warming footprint. *Geophys. Res. Lett.*, **41**, 3220–3226, <https://doi.org/10.1002/2014GL059748>.
- Williams, A. P., R. Seager, J. T. Abatzoglou, B. I. Cook, J. E. Smerdon, and E. R. Cook, 2015: Contribution of anthropogenic warming to California drought during 2012–2014. *Geophys. Res. Lett.*, **42**, 6819–6828, <https://doi.org/10.1002/2015GL064924>.
- Woodhouse, C. A., and J. T. Overpeck, 1998: 2000 years of drought variability in the central United States. *Bull. Amer. Meteor. Soc.*, **79**, 2693–2714, [https://doi.org/10.1175/1520-0477\(1998\)079<2693:YODVIT>2.0.CO;2](https://doi.org/10.1175/1520-0477(1998)079<2693:YODVIT>2.0.CO;2).
- , G. T. Pederson, K. Morino, S. A. McAfee, and G. J. McCabe, 2016: Increasing influence of air temperature on upper Colorado River streamflow. *Geophys. Res. Lett.*, **43**, 2174–2181, <https://doi.org/10.1002/2015GL067613>.